Hindawi Publishing Corporation
Journal of Crystallography
Volume 2016, Article ID 4351347, 11 pages
http://dx.doi.org/10.1155/2016/4351347

Research Article

Finite Element Simulation and X-Ray Microdiffraction Study of Strain Partitioning in a Layered Nanocomposite

R. I. Barabash,[1] V. Agarwal,[2] S. Koric,[2,3] I. Jasiuk,[2] and J. Z. Tischler[4]

[1]*Materials Science and Technology Division, Oak Ridge National Laboratory, Oak Ridge, TN 37831, USA*
[2]*Mechanical Science and Engineering Department, University of Illinois at Urbana-Champaign, Urbana, IL 61801, USA*
[3]*National Center for Supercomputing Applications, University of Illinois at Urbana-Champaign, Urbana, IL 61801, USA*
[4]*Advanced Photon Source, Argonne National Laboratory, Argonne, IL 60439, USA*

Correspondence should be addressed to R. I. Barabash; rbarabas@utk.edu and I. Jasiuk; ijasiuk@illinois.edu

Received 28 February 2016; Accepted 4 May 2016

Academic Editor: Laszlo Toth

The depth-dependent strain partitioning across the interfaces in the growth direction of the NiAl/Cr(Mo) nanocomposite between the Cr and NiAl lamellae was directly measured experimentally and simulated using a finite element method (FEM). Depth-resolved X-ray microdiffraction demonstrated that in the as-grown state both Cr and NiAl lamellae grow along the ⟨111⟩ direction with the formation of as-grown distinct residual ~0.16% compressive strains for Cr lamellae and ~0.05% tensile strains for NiAl lamellae. Three-dimensional simulations were carried out using an implicit FEM. First simulation was designed to study residual strains in the composite due to cooling resulting in formation of crystals. Strains in the growth direction were computed and compared to those obtained from the microdiffraction experiments. Second simulation was conducted to understand the combined strains resulting from cooling and mechanical indentation of the composite. Numerical results in the growth direction of crystal were compared to experimental results confirming the experimentally observed trends.

1. Introduction

Strain partitioning is the most important phenomenon responsible for unique properties of composites [1–7]. The role of interfaces in strain partitioning in composites was emphasized by a number of authors [8, 9]. In particular, Ni-based [3] and especially NiAl-based composites are the focus of current research because they can operate at high temperatures (up to 1300°C) in corrosive environments [10–17]. They can be used for high temperature applications including structural components in energy conversion facilities, for example. It was shown that small additions of Mo (up to 6 at%) change the morphology of the Cr phase from rod-like to lamellar [11, 18]. Therefore, NiAl/Cr(Mo) system has recently attracted attention because both phases grow into lamellae during crystallization [10, 11, 18–22]. However, the mechanism of strain partitioning in these alloys and the role of interfaces in load transfer from one phase to another are still poorly understood. These open issues provided motivation for this study.

Spherical indentation is one of the possible techniques to study the strain partitioning under loading in these alloys. The advantage of using spherical indentation as compared to uniaxial tension/compression measurements is that during indentation the deformation is changing from the maximum under an indent to zero in the area not affected by the indentation. Therefore, all information about the indentation-induced strain partitioning is confined in a relatively small volume which can be both assessed experimentally and simulated with FE. The spherical shape of the indent was chosen in order to prevent the interplay between the specific shape of the indent with the crystal lattice anisotropy.

2. Materials and Experimental Procedures

2.1. Growth of NiAl/Cr(Mo) Eutectic Alloys. The NiAl-Cr phase diagram has a eutectic composition at 34 at% Cr at the temperature T_{eut} = 1450°C. The eutectic temperature is lower than the melting temperature of Cr (T = 1880°C) and

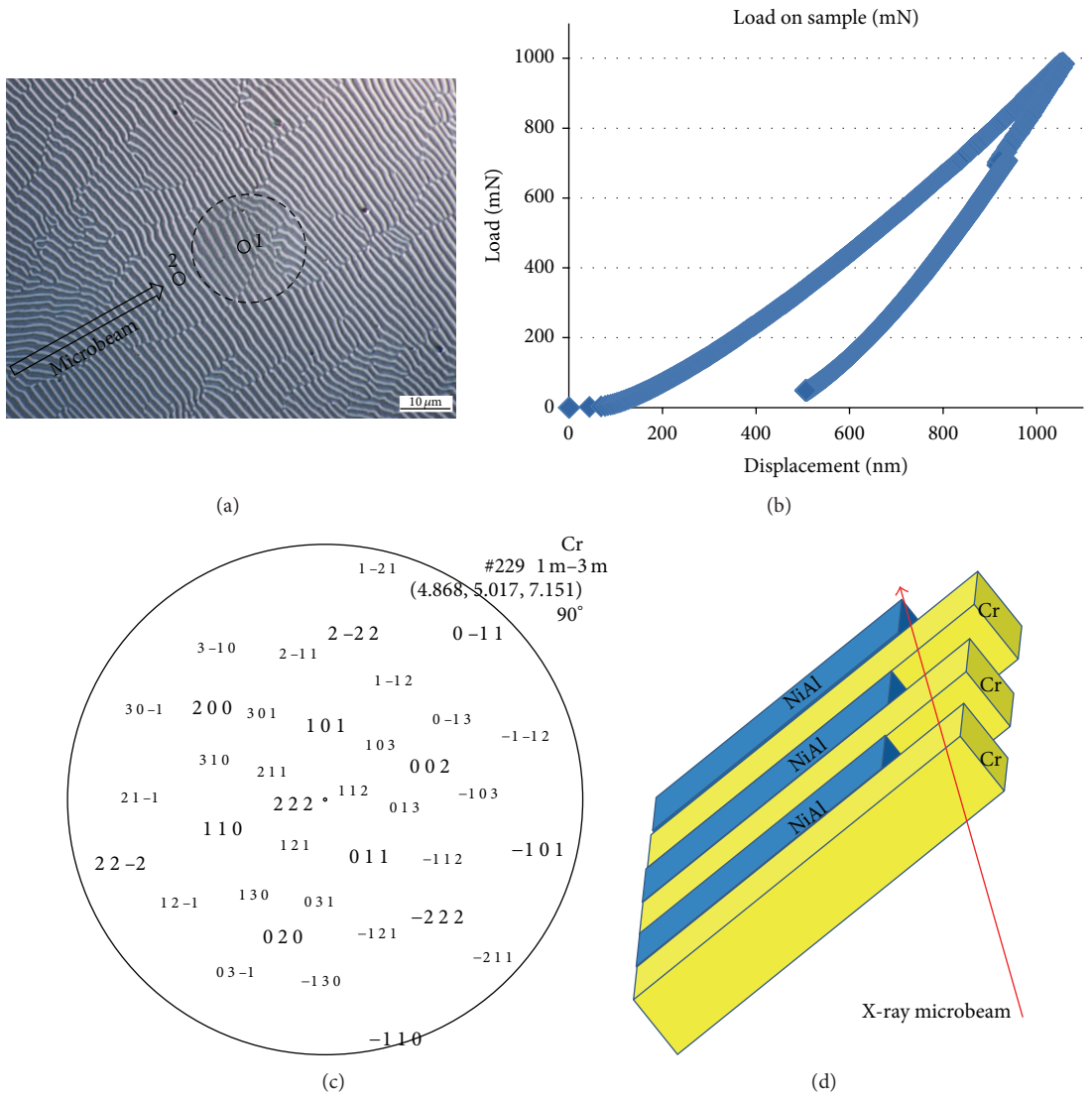

Figure 1: (a) SEM image of the indented area with Cr lamellae in NiAl matrix chosen for DAXM measurements. The growth direction of both lamellae kinds is along ⟨111⟩ direction. The direction of the beam trajectory intercepting the sample surface at 45° is shown by an arrow. Depth-resolved DAXM measurements of the indented sample were performed for locations 1 and 2. (b) Load-displacement curve during the indentation. The main parameters of the load-displacement curve, maximum force and displacement during indentation, were further used in simulations. (c) Stereographic projection showing that growth is along ⟨111⟩ crystallographic direction. The different fonts of the crystallographic indices on the figure refer to different symmetry of crystallographic directions. Larger indices correspond to higher symmetry directions. For example, the ⟨222⟩ direction corresponds to growth direction that is almost in the center of the projection, and other directions from the same family, that is, [2, 2, −2], [2, −2, 2], and [−2, 2, 2] are of the same size. (d) Geometry of the X-ray microbeam intercepting different NiAl and Cr lamellae with depth.

of NiAl (T = 1674°C) [13]. The elastic moduli of pure NiAl and Cr single crystals along the ⟨111⟩ directions are 277 and 248 GPa, respectively [11]. The lattice parameters mismatch is ~0.1%. In this study, the NiAl/Cr alloys were additionally alloyed by 3 at% Mo to obtain a lamellar microstructure of the composite. Therefore, the lattice parameters of the NiAl and Cr(Mo) lamellae were measured in this study before indentation. The NiAl/Cr(Mo) samples were directionally crystallized leading to the formation of the well-aligned NiAl and Cr lamellae (Figure 1(a)). The details of the alloy preparation and eutectic growth can be found elsewhere [10, 11]. The spacing and relative size of lamellae depend on the growth rate and composition, and under the conditions of this experiment, they resulted in approximately parallel lamellae with nearly equal thickness with periodicity of ~1.2 μm. Cr (3% Mo) lamellae have a BCC structure while intermetallic NiAl lamellae have an ordered CsCl-type B2 structure [5]. Both NiAl and Cr (3% Mo) lamellae grow along the ⟨111⟩ direction, forming heterointerfaces parallel to $(\bar{1}\,\bar{1}2)$ type planes in both phases [11]. Mo is mainly found in

the Cr lamellae, although small traces of Mo are also present in NiAl lamellae. Thus, lattice parameters of the two lamellae types differ from those of pure NiAl and Cr.

Sample preparation was as follows. Samples were cut from a directionally solidified Cr(Mo)-NiAl eutectic rod perpendicular to the growth direction (cross section), mounted in epoxy, and then polished. Two kinds of samples were prepared: (1) in the first sample, the matrix was etched away at the depth of ~5 μm; this sample was used to determine residual as-grown stresses in the lamellae; (2) the second sample was only slightly etched (several nm) to reveal the microstructure (Figure 1(a)). This sample was further indented and studied for strain partitioning between lamellae. The orientations of the lamellae along the growth direction were determined from the Laue pattern.

The alternating Cr/NiAl lamellae are visible on the scanning electron microscopy (SEM) image of the sample cross section (Figure 1(a)). The orientation of the surface normal was along the [111] direction for both Cr and NiAl lamellae.

2.2. Indentation. Spherical indentation on the polished surface perpendicular to the growth direction was conducted with an MTS Nano Indenter XP equipped with a sapphire tip with radius of 100 μm to a prescribed load of $P = 1{,}000$ mN. Load-displacement curves were recorded for each indentation (Figure 1(b)). The maximum force during indentation reached 1,000 mN and the displacement during indentation did not exceed 1100 nm. These parameters were further used in simulations of the indentation-induced deformations.

2.3. Depth-Resolved X-Ray Strain Microscopy. Synchrotron polychromatic X-ray microdiffraction (PXM) was performed at the 34ID-E beamline of the Advanced Photon Source at the Argonne National Laboratory with a focused ~0.3 × 0.4 μm beam with an energy-dependent penetration depth ~30–50 μm. The energy range of the polychromatic microbeam was within 5–27 keV. PXM allowed studying orientation spread within the irradiated volume using a modified Laue technique. The experimental setup of the beamline permits moving the monochromator into the beam and working with monochromatic radiation as well. Measurements with monochromatic radiation provide information about dilatational strain gradients. Measurements with both polychromatic (Laue) and monochromatic radiation were performed. In this setup, the X-ray microbeam intercepts the sample surface at ~45° and penetrates into the depth of the NiA/Cr(Mo) sample reaching ~50 μm. Therefore, the diffracted radiation integrates inputs from all depths and lamellae intercepted by the beam. To disentangle this depth-integrated intensity and to obtain depth-resolved information about individual submicron-size lamellae, a special differential-aperture X-ray microscopy (DAXM) technique was applied [11, 23–27]. With the DAXM technique, a platinum wire with a diameter of ~50 μm serves as a differential aperture. During the depth-resolved measurements, the wire is moving parallel to the sample surface in the diffracted radiation field and shadows portion by portion the Laue patterns, depending on the relative position of the wire and the sample surface. Typically, for each measured location, about ~400 partially shadowed images are taken. Together with initial depth-integrated Laue pattern, these 400 patterns are analyzed using a ray-tracing algorithm. As a result, complete depth-resolved information on the intensity from each micrometer of depth is recovered.

The DAXM technique can be performed using a polychromatic (PDAXM) or monochromatic (MDAXM) radiation [28]. Both techniques allow obtaining information with a 1 μm depth resolution. PDAXM reveals lattice orientation gradients with depth, while MDAXM gives information about dilatational strain gradients with depth. In order to perform MDAXM measurements, first the complete Laue pattern should be obtained and indexed using a depth-integrated PXM. After indexation, the energy corresponding to a maximal intensity of the specific h, k, l reflection, E_{hkl}, is determined and is used as a mean energy for the energy-scans. The energy-scan can be performed in steps within the above energy range around the mean E_{hkl} value. Furthermore, for each energy value, the depth-resolved measurements with platinum wire were performed. Such depth-resolved energy-scans, MDAXM, provided unique detailed information about the phase-specific dilatational strain gradient with depth. Both PDAXM and MDAXM were used in this study.

For spherical indentation, it is important that the depth-resolved X-ray strain microscopy allows for resolving strains with 1 μm steps in the depth along the beam path. The 0.3 × 0.4 μm size of the beam is smaller than the thickness of individual lamellae allowing for resolving strain information separately from NiAl and Cr lamellae. The characteristic length of strain changes, so-called "slip zone," typically extends over 10–20 μm in depth. Therefore, the 1 μm step size gives a unique possibility of measuring the depth-resolved strain gradients and further compare them with strains obtained using FE simulations.

3. Results and Discussion

3.1. Residual as-Grown Stresses. An SEM image of the cross section of the sample shows alternating NiAl and Cr lamellae with the total thickness of 1200 nm (Figure 1(a)). The area of the indent is marked by a dashed circle (Figure 1(a)). Stereographic projection obtained from an undeformed region with PDAXM method (Figure 1(c)) unambiguously indicates that both kinds of lamellae grow along the [111] crystallographic direction. Both NiAl and Cr lamellae contain small amounts (up to 3%) of Mo which affects the value of the lattice spacing. The reference samples for these compositions of lamellae cannot be prepared and measured independently because the melting point of Mo is much higher than, for example, the boiling point of Al. Therefore, it is practically impossible to prepare these compositions without crystallizing a composite. In order to determine strains in the composite constituents, it was necessary first to measure the strain-free lattice spacing of both phases as they differ from theoretical values for pure NiAl and Cr. With the synchrotron PXM and DAXM measurements, the differences of the reciprocal lattice spacings for h, k, l reflection, Q_{hkl}, are determined more precisely than their absolute values. The reciprocal lattice

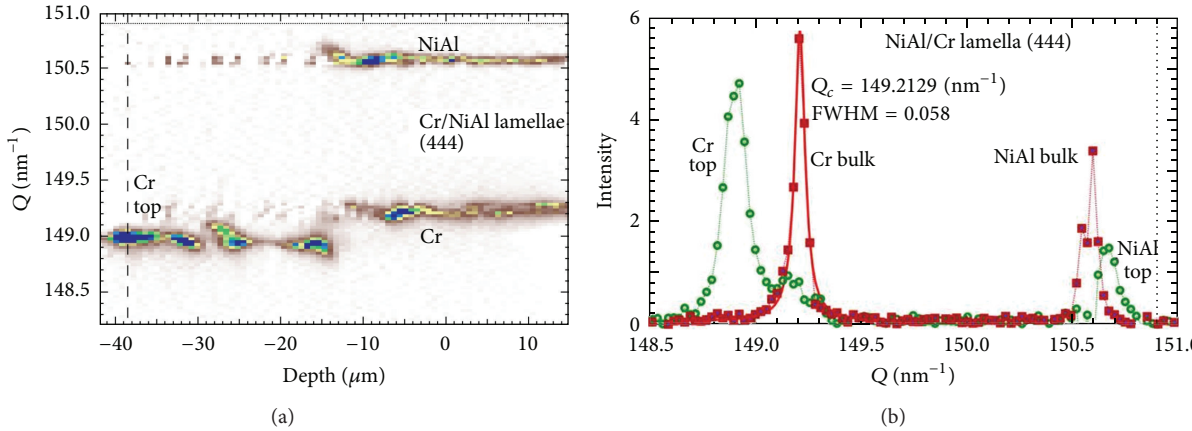

FIGURE 2: (a) Depth-resolved reciprocal lattice spacing Q_{444}-distribution measured in the energy interval for 4, 4, 4 reflection. (b) Line profiles corresponding to the stress-free NiAl and Cr lamellae at the surface (green open circles) and in the bulk of the composite (red filled squares). Thin vertical line in (b) is the theoretical value of the reciprocal lattice spacing taken from the literature for pure NiAl. The measured relaxed NiAl (Mo) lattice parameter differs from the one for pure NiAl due to the presence of Mo.

spacings of the NiAl and Cr(Mo) are relatively close and it was possible to measure them simultaneously in one scan, which essentially improved the accuracy of the result. To get information about the possible as-grown residual strains, the depth-resolved reciprocal lattice spacings were measured with MDAXM in the first sample, where matrix was etched away at the depth of ~5 micrometers. As both lamellae kinds grow along the ⟨111⟩ crystallographic direction, the 4, 4, 4 reflection for both lamellae kinds was chosen to study the strain gradients. The 4, 4, 4 reflections for both NiAl and Cr(Mo) lamellae are close in both the orientation space and their absolute values. The relatively small difference between the NiAl and Cr inverse lattice spacing, corresponding to 4, 4, 4 reflection, allowed for measuring both of them in one scan. Therefore, the mean energy value for this energy-scan was chosen in the middle between the energies corresponding to the NiAl and Cr 4, 4, 4 reflections. The energy of the beam was scanned in the range corresponding to the 4, 4, 4 reflection with a step of 3 eV for both samples within the range of keV including the reflections for both phases (Figure 2(a)). The small X-ray beam size (<0.5 μm) allowed nondestructive measurements of lattice rotations and strains in the individual phase-specific mesoscale lamellae at different depths. The protruding out of the matrix Cr(Mo) lamellae are strain/stress-free. The beam coming at 45° to the sample surface is intercepting Cr(Mo) lamellae one-by-one as it penetrates the sample (Figure 1(d)). First, the beam probes several Cr(Mo) lamellae tops before penetrating the depth of the sample. All of them are stress-free and have the same strain-free reciprocal lattice spacing distinct from the bulk value. It results in the plateau of Q values at Q_{444} = 148.9 nm^{-1} corresponding to the strain/stress-free 4, 4, 4 reciprocal lattice spacing of Cr(Mo) lamellae (Figure 2(a)). Initially, in this depth region, the zero intensity is diffracted from NiAl, as the matrix is etched away. Therefore, no signal from the NiAl matrix is observed in the area of etched matrix. Eventually, the beam is penetrating into the depth of the sample probing simultaneously Cr and NiAl lamellae (Figure 1(d)). In the bulk of the composite, the NiAl and Cr(Mo) lamellae constrain each other and have distinct constrained 4, 4, 4 reciprocal lattice spacings (Figures 2(a) and 2(b)). As the thickness of lamellae is less than a micron, the intensity diffracted by both lamellae kinds alternates. This relates to two other plateaus of Q values with depth determined by the as-grown strained value of the 4, 4, 4 reciprocal lattice spacing for both kinds of lamellae at Q_{444} = 149.2 and Q_{444} = 150.6 nm^{-1} for Cr(Mo) and NiAl lamellae, correspondingly. Line profiles corresponding to the two distinct depths are shown in Figure 2(b). One profile (green open circles) corresponds to the near-surface stress-free values for both lamellae kinds, while another one (red filled squares) corresponds to deep bulk values for both phases (Figure 2(b)). The level of residual as-grown stresses estimated from the difference between these two values results in a 0.16% compressive stress for the Cr(Mo) lamellae and almost three times smaller, ~0.05%, tensile stress for the NiAl matrix. These values are almost an order of magnitude smaller than those in the NiAl/Mo composite [12].

3.2. Axial Texture. Indentation-induced strain partitioning was studied on the second sample without etching of the NiAl matrix. While both kinds of lamella grow along the [111] direction, an axial texture is observed in the cross section. It is visible on both the SEM image of the cross sections (Figure 1(a)) and the pole figure calculated from the white-beam diffraction for the (111) pole (Figure 3(a)). The in-plane direction of the lamellae colonies slightly varies from colony to colony. The axial texture also varies with depth which is indicated by a different color of the three-dimensional (3D) slice of the sample (Figure 3(b)). Each color at this figure corresponds to a different orientation. The purple color corresponds to one colony of lamellae which was chosen for the analysis and represents mainly the area unaffected by the indentation. Deeper, below this colony,

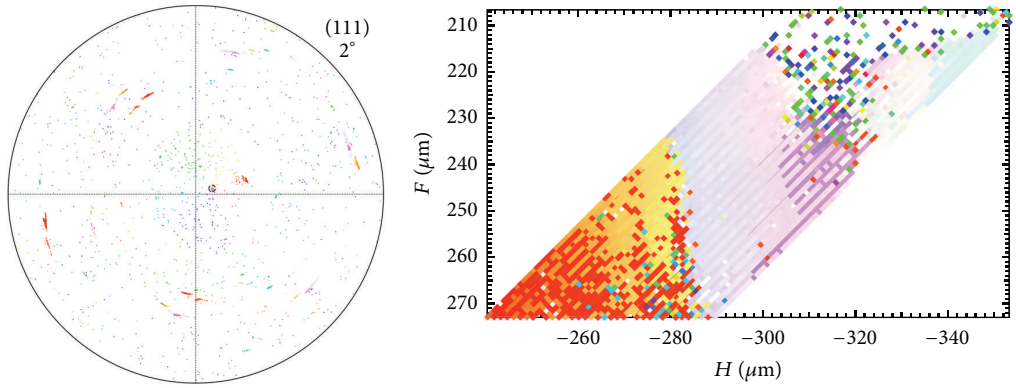

(a) (b)

FIGURE 3: (a) Pole figure of the sample cross section shows sharp ⟨111⟩ texture. (b) Depth-resolved 3D orientation map in the indented area.

an orange color corresponds to the lamellae colony with a different orientation. Both purple and orange colors refer to the colors at the inverse pole figure (Figure 3(a)). Above the purple grain, no definitive orientation can be detected; different colors are all mixed; this corresponds to the highly deformed near-surface indented area.

The triple junction between the three colonies was chosen for indentation to compare if there is any significant dependence of the depth-resolved strain-gradients partitioning on the axial reorientation between different colonies. The indented area was first mapped in 3D with depth-resolved white-beam measurements and the regions of the largest deformation were found, region of mixed colors (Figure 3(b)). The probed area corresponds to the colony marked with purple color underneath the indent. In the most damaged near-surface indented area, the orientation of the affected lamellae changes stochastically and does not show any definitive orientation indicated by different colors.

3.3. Indentation-Induced Strain Partitioning along the Growth Direction between the Cr and NiAl Lamellae. Strain partitioning was characterized by 3D depth-resolved monochromatic measurements of the 4, 4, 4 reciprocal lattice spacing with the X-ray microbeam probing the sample along the two beam paths marked as (1) and (2) in Figure 1(a). The measurement starting at location 1 is taken in the most affected area while measurement starting at location (2) probes mostly unaffected area and is used as reference.

The measured misfit between the two lamellae along the [111] growth direction in the strain-free near-surface region is ~1.6%, while in the bulk of the composite it is ~0.86% due to residual strains.

Starting at location 1, the beam intercepts the sample surface in the area of largest deformation near the center of the indent (Figure 1(a)). Depth-dependent Q_{444} reciprocal lattice spacing measurements for Cr solid solution and NiAl lamellae (Figure 4(a)) demonstrate distinct signs and amplitudes of strain distributions between these two phases: the NiAl Q reciprocal lattice spacing decreases ~0.26% near the surface revealing that the near-surface deformed NiAl lamellae are slightly under compression. At the same deformed location, the Cr lamellae are under tension compared to the bulk composite value for Cr. The Cr lattice parameter in the affected region is 0.47% larger than that in the bulk of the composite (Figure 4(b)). Tensile strains in the Cr lamellae first slightly increase with depth and reach their maximum value of ~0.54% at a depth of 6 μm; then, the strain amplitude decreases, and at a depth of ~20 μm, they saturate at their undeformed bulk values for both lamellae phases.

The observation of distinct sign and amplitude strain distributions in the neighboring Cr and NiAl lamellae likely depends on the ratio between the elastic moduli of the Cr and NiAl neighboring lamellae and on the existing as-grown residual stresses.

3.4. Numerical Implementation and Computational Challenges: Simulation of Indentation in NiAl-Cr Composite. In parallel with the experiments described above, finite element simulations were conducted in order to compute residual strains and indentation-induced strains in the NiAl-Cr composite. 3D numerical simulations were carried out with the implicit finite element method (FEM) using a software Abaqus/Standard [29].

In order to identify the optimum mesh size, a mesh refinement study was performed. The domains were discretized using 20-node quadratic hexahedral elements with two levels of refinement: coarse and refined. The coarse mesh had more than 730,000 degrees of freedom (DOFs), while the refined mesh had almost 5 million DOFs. Material nonlinearities arising from anisotropic plastic material properties, geometric nonlinearities from large deformations, and complex contact conditions lead to increased ill-conditioning due to the element shape distortion in the mesh refinement. This made the numerical analysis of the refined model extremely difficult even on the latest high performance computing platforms. Within each quasistatic time step, a system of nonlinear equations was linearized and solved with a Newton-Raphson (NR) iteration scheme [30, 31] in Abaqus which

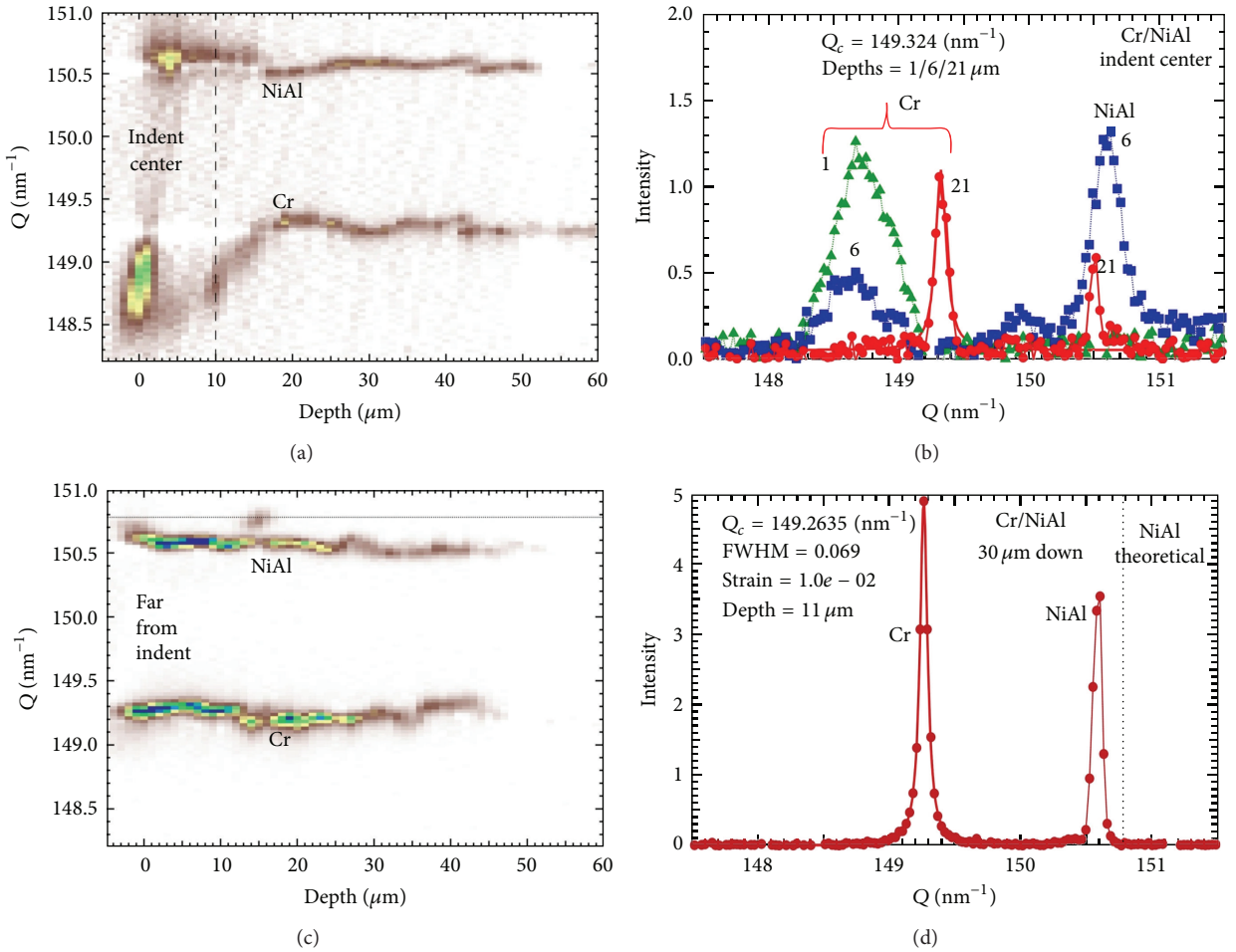

FIGURE 4: ((a), (b)) Depth-resolved 4, 4, 4 reciprocal lattice spacing for beam path starting in location 1 in the center of the indented area (a) and corresponding line profiles at three distinct depths marked by numbers (b). ((c), (d)) Depth-resolved 4, 4, 4 reciprocal lattice spacing for beam path starting in location 2 outside of the indented area (c) and corresponding line profiles (d) which practically do not change with depth.

required several linear solver solutions or global equilibrium iterations. Due to the complexity of this problem (material and geometric nonlinearities, three-dimensional problem involving multiple layers, and complex boundary conditions), the direct multifrontal solver in Abaqus/Standard with hybrid parallelization was used. Koric et al. [32] have recently showed that this type of solver has enough scalability and robustness to perform computations on large ill-conditioned problems on many hundreds of cores. In this approach, its hybrid Message Passing Interface (MPI)/Threaded implementation can take full advantage of large amount of memory and modern multicore processors. It is known that the wall clock time for direct solution of sparse symmetric systems is approximately proportional to the square of the number of unknowns or degrees of freedom (DOFs) [33]. While this is somewhat offset by a more efficient parallel execution on larger domains, it still imposes a severe restriction on the size of the domain that can feasibly be modeled with highly nonlinear quasistatic problems even on the latest supercomputing platforms. Whereas the coarse mesh size takes 7 hours on 6 computational nodes (120 CPU cores), the refined case would require more than two weeks of dedicated supercomputer time on 15 computational nodes (300 CPU cores).

We used the high performance computing (HPC) cluster called iForge [34]. The iForge computer at the National Center for Supercomputer Applications at the University of Illinois at Urbana-Champaign is specifically built and tuned to accelerate some of the toughest industrial HPC workflows. The current configuration consists of 144 dual socket Dell PowerEdge M620 nodes, each with two Intel Xeon E7 4890v2 CPUs (Ivy Bridge) and 20 cores operating at 2.8 GHz and 256 GB of RAM. They are connected with QDR Infiniband networking fabric.

3.4.1. Initial Thermomechanical Simulations. The geometry used for simulations of residual stresses and indentation consisted of a rectangular block of dimensions 10 μm × 10 μm × 5.6 μm. Alternating layers of NiAl and Cr, 0.8 μm and 0.4 μm thick, respectively, were modeled by partitioning the block into parallel layers, as shown in Figure 5. Layers

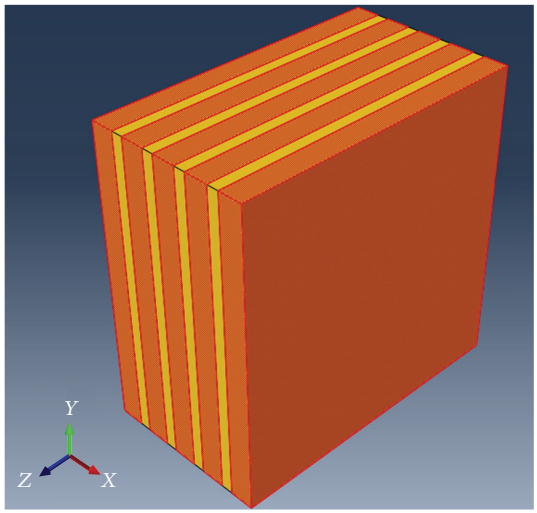

Figure 5: Geometry of the model used for finite element simulations.

Table 1: Elastic moduli and thermal expansion coefficients for NiAl and Cr lamellae.

	c_{11} (GPa)	c_{12} (GPa)	c_{44} (GPa)	α (K^{-1})
NiAl	198	137	116	15.3×10^{-6}
Cr	350	68	101	4.9×10^{-6}

were assumed to be perfectly bonded to each other with no possibility of delamination. The domain was meshed using cubic elements of size 0.1 μm (Figure 5).

Layers were assumed to have cubic symmetry to match the experimental results and were given different anisotropic elastic properties, shown in Table 1. The z-direction in simulations corresponded to the [111] direction for both crystal layers and it was also the direction of growth. The y-direction, which is the normal to the probed surface, was oriented along the $[\bar{1}\,\bar{1}2]$ direction. Local coordinate system was defined accordingly to provide direction specific elastic constants.

Thermal expansion coefficients were assumed to be constant over the temperature range used for simulations. Elastic moduli and thermal expansion coefficients are given in Table 1. The z-symmetry boundary conditions were applied to the model as the block was cooled down from 1400°C to 0°C.

Strains in the direction of crystal growth (along the z-axis) were the focus of the analysis. It was observed that NiAl lamellae were under forward compressive stresses whereas Cr lamellae were under tensile back stress (Figure 6). Away from the boundaries, strains in both the layers were fairly uniform, giving a value of 0.19% in NiAl and −0.047% in Cr. The strains were visualized on the plane of symmetry of the model.

X-ray diffraction studies have suggested strain values of 0.1% and −0.025% in NiAl and Cr, respectively. It was observed that cooling the model in simulations from 700°C to 0°C yielded strain values very close to the experimental values.

3.4.2. Thermal Simulation Followed by Indentation. From initial simulations, it was established that, to obtain the residual

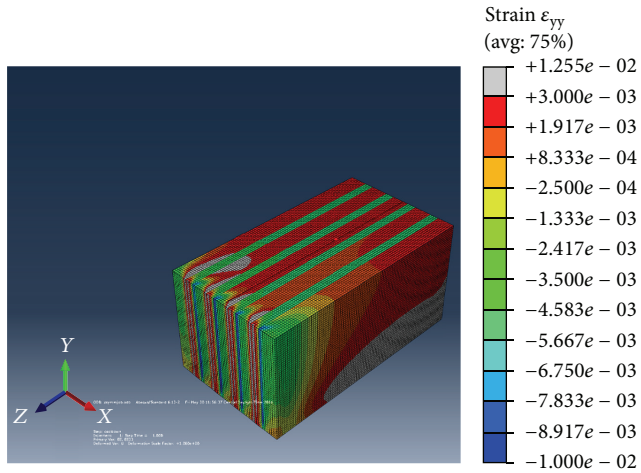

Figure 6: Simulated elastic thermal strains show that NiAl lamellae are under forward compressive stresses whereas Cr lamellae are under tensile back stress in agreement with experiment.

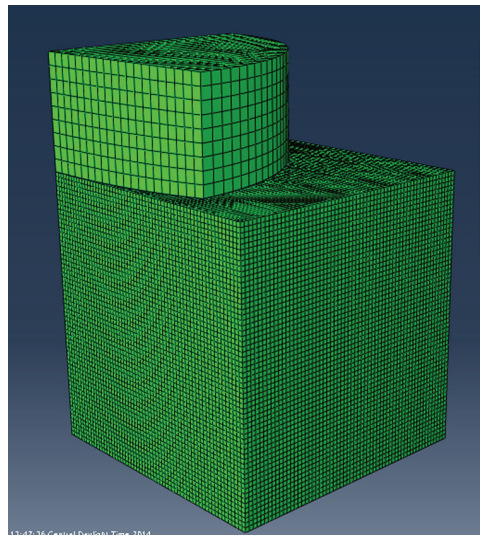

Figure 7: Model for thermal simulation followed by indentation.

strain state of NiAl-Cr, the finite element model should be run assuming cooling down by about 700°C. Then, a second simulation which included thermal and indentation steps was conducted. Residual thermal strains were generated by cooling the model by 700°C, followed by indentation.

In the simulations, the geometry consisted of two parts: composite cubic block with edge length 12 μm and indenter of radius 100 μm. Composite block had similar properties as adopted in the earlier model. Only a quarter of the block and indenter were modeled and symmetric boundary conditions were imposed (Figure 7). Direction of the growth or the z-direction corresponds to [111] orientation for both crystals. Simulations were performed for the two distinct orientations of the indentation direction: (1) The normal to the surface on which indentation was performed (y-direction) was oriented along the $[\bar{1}\,\bar{1}2]$ direction; (2) the indentation was performed

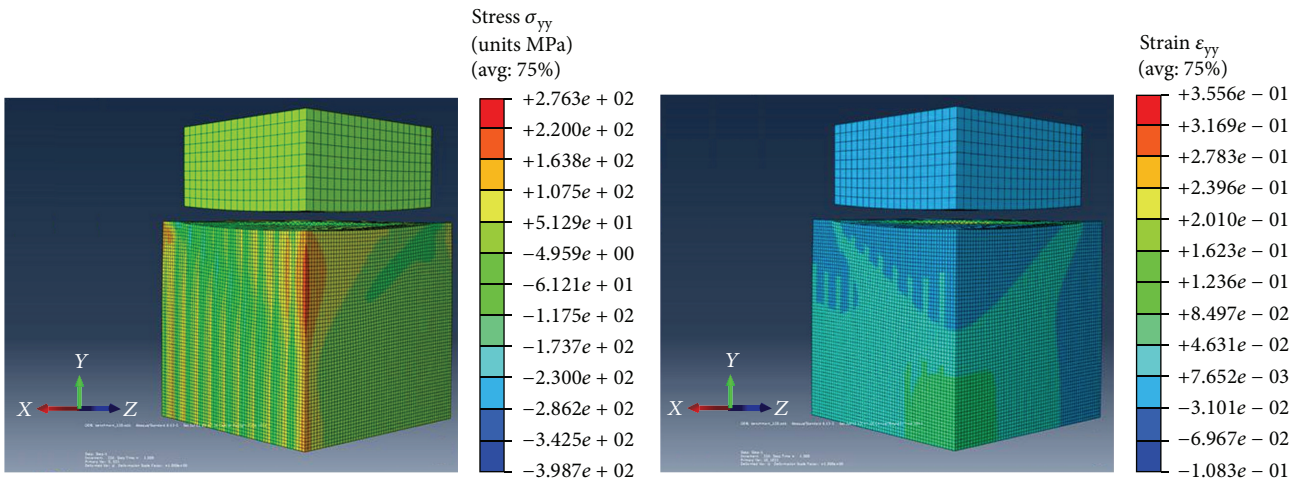

Figure 8: (a) Simulated stresses along the growth direction and (b) simulated true strains in the growth direction, both after indentation.

along the [111] direction coinciding with the growth direction. The same elastic constants were adopted for the model as in the previous simulation and a constant yield stress of 200 MPa was used for both materials to denote the unset of plastic deformation.

In the thermal step, the model was cooled down from 700°C to 0°C, followed by an indentation step, in which the indenter was pushed into the block by 1 μm at a constant velocity, followed by retraction of indenter at the same velocity.

As stated before, two different element sizes were used for meshing, 0.1 μm and 0.2 μm, and results were analyzed. It was observed at the end of the thermal step as well as at 10% of the indentation step that the coarser mesh resulted in very similar strain results as the finer mesh. Thus, the problem was fully solved with a coarser mesh. The coarser mesh was used for further simulations.

3.5. Comparison between the Simulations and Experimental Results. In the 3D simulations during loading, the crystal under indent within the half of the contact radius yields first and the plastic zone increases with applied load. Resulting elastic stress field in the simulations has an arc-like shape centered near the contact center. After unloading in the simulations, the plastically deformed material in the area affected by indentation tends to preserve its shape in the simulations, while the surrounding elastic material springs back and transmits compressive stress into the plastic zone. However, in contrast to the indentation of the single phase materials, the residual as-grown stresses, which are already present in the bulk of the composite material, overlap with the indentation-induced stresses and are partitioned between the two phases of the composite material. As a result, after simulation of cooling and indentation of the composite, it was observed that the NiAl and Cr lamellae were in different stress states than those before indentation. The NiAl lamellae were under forward compressive stresses along the direction of growth

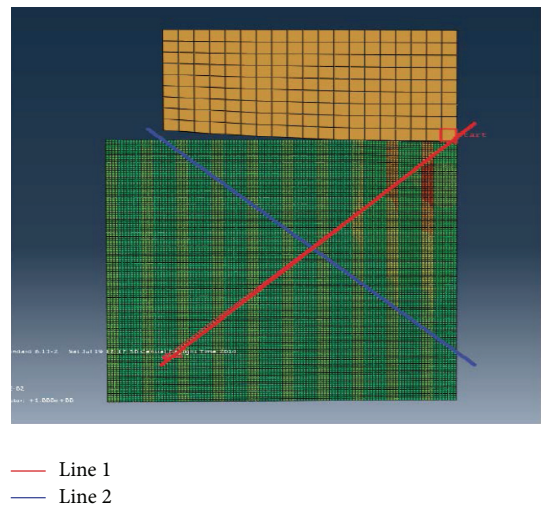

Figure 9: Position of lines 1 and 2 for simulation of depth-dependent phase-specific strains in Cr and NiAl lamellae.

whereas the Cr lamellae were under backward tensile stresses in agreement with the experiment; compare Figure 8(a) to Figure 4(a). Moreover, the 3D simulation of indentation along different crystallographic directions shows difference in the amplitude of the indentation-induced strains in both phases. For a better comparison between the simulated and experimental results, the strain distribution along the specific lines was extracted from the simulations and compared to the experimental strain distribution along the same lines.

Figure 9 shows the positions of the two lines (1 and 2) in the simulated model corresponding to the experimentally measured intensities along the similar lines shown in Figure 4. Because of the large volume needed for simulations, only a quarter of the indented volume was simulated assuming that strains around the spherical indent are symmetric. To obtain strains along the line starting at the very center of

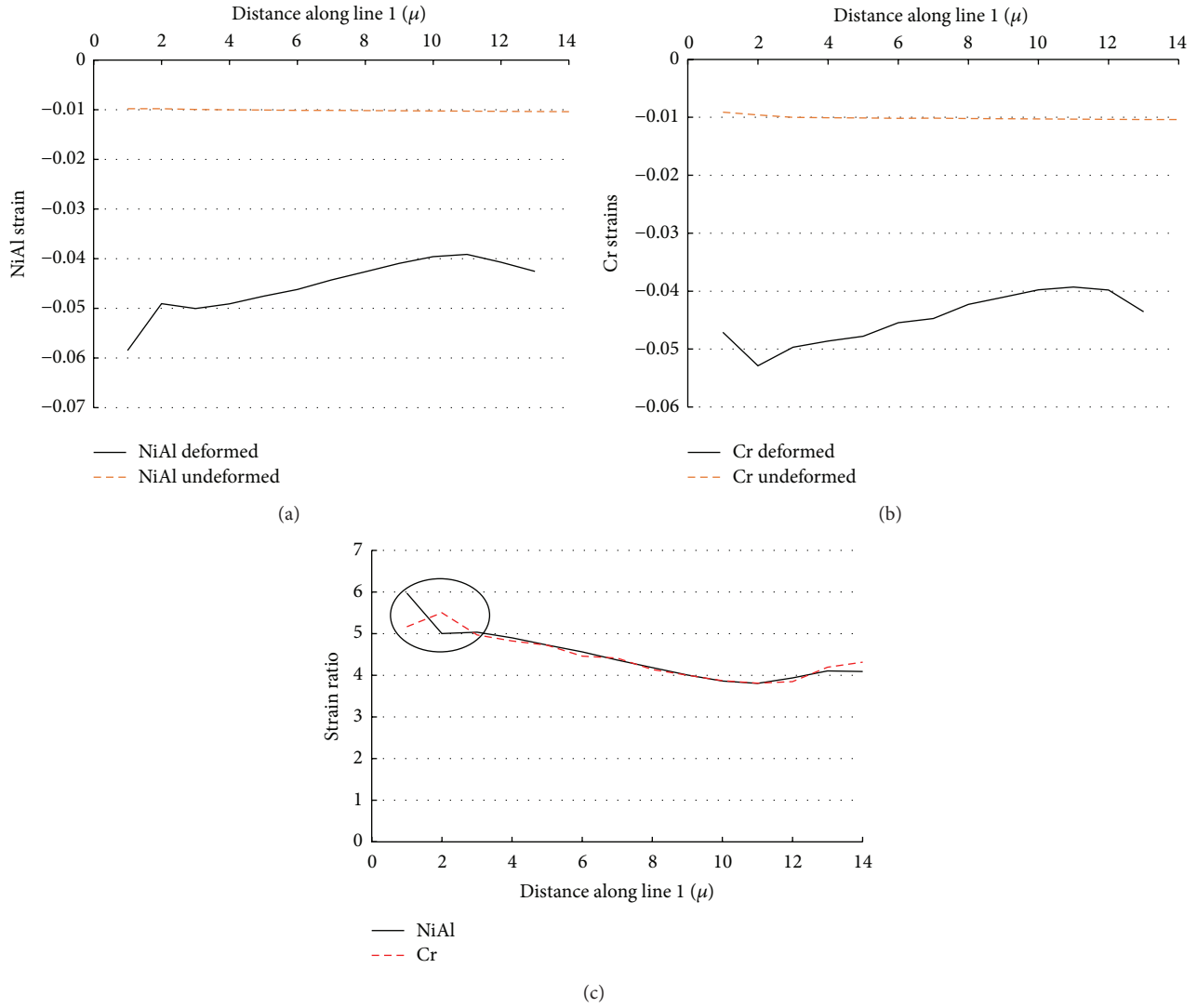

FIGURE 10: Strains and strain ratio for Cr and NiAl lamellae along line 1 shown in Figure 9: (a) strain in an NiAl layer as a function of position; (b) strain in a Cr layer as a function of position; (c) strain ratio for NiAl and Cr lamellae as a function of position.

the indented area, line 1 was chosen. To obtain strains along the line starting 10 μm from the indented center, the strains were calculated along line 2. The simulated depth-dependent strains along these lines, 1 and 2, are shown in Figures 10 and 11. The strains in both lamellae kinds were calculated for indented (deformed) and not indented (undeformed) states. The ratio was calculated using the undeformed state as a reference for each state. Near the surface for line 1, the simulated strains demonstrate the change in the strain sign for both phases (Figure 10). For Cr lamellae near the surface, the strains are positive and then turn to negative at the depth of approximately 3 μm. For NiAl, the strain dependence on depth is more complicated. For line 1, the strains are negative near the surface; then, they turn to positive at the short distance in depth and then turn negative again. For line 2, the simulated strains are negative in NiAl and positive in Cr lamellae near the surface (Figure 11). These trends confirm the experimentally observed results (Figure 4). The strain ratio calculated for strain values of the indented (deformed) relative to the initial undeformed state at the same depth was calculated for both lines (Figures 10 and 11). The simulated results unambiguously show that near the surface in the most deformed area the strain ratio for NiAl and Cr demonstrates distinct trends as those observed experimentally (Figure 4).

4. Conclusions

We find that in the NiAl/Cr(Mo) nanocomposite the indentation-induced strain partitioning between the individual lamellae results in alternating tensile/compressive strains in the submicron-size Cr and NiAl lamellae. 3D simulations confirm the experimentally observed alternating tensile/com pression strains in the neighboring Cr and NiAl lamellae. Formation of these regions can be understood as a result of the compatibly constrained lamellae deformations and load partitioning through the interfaces between the harder

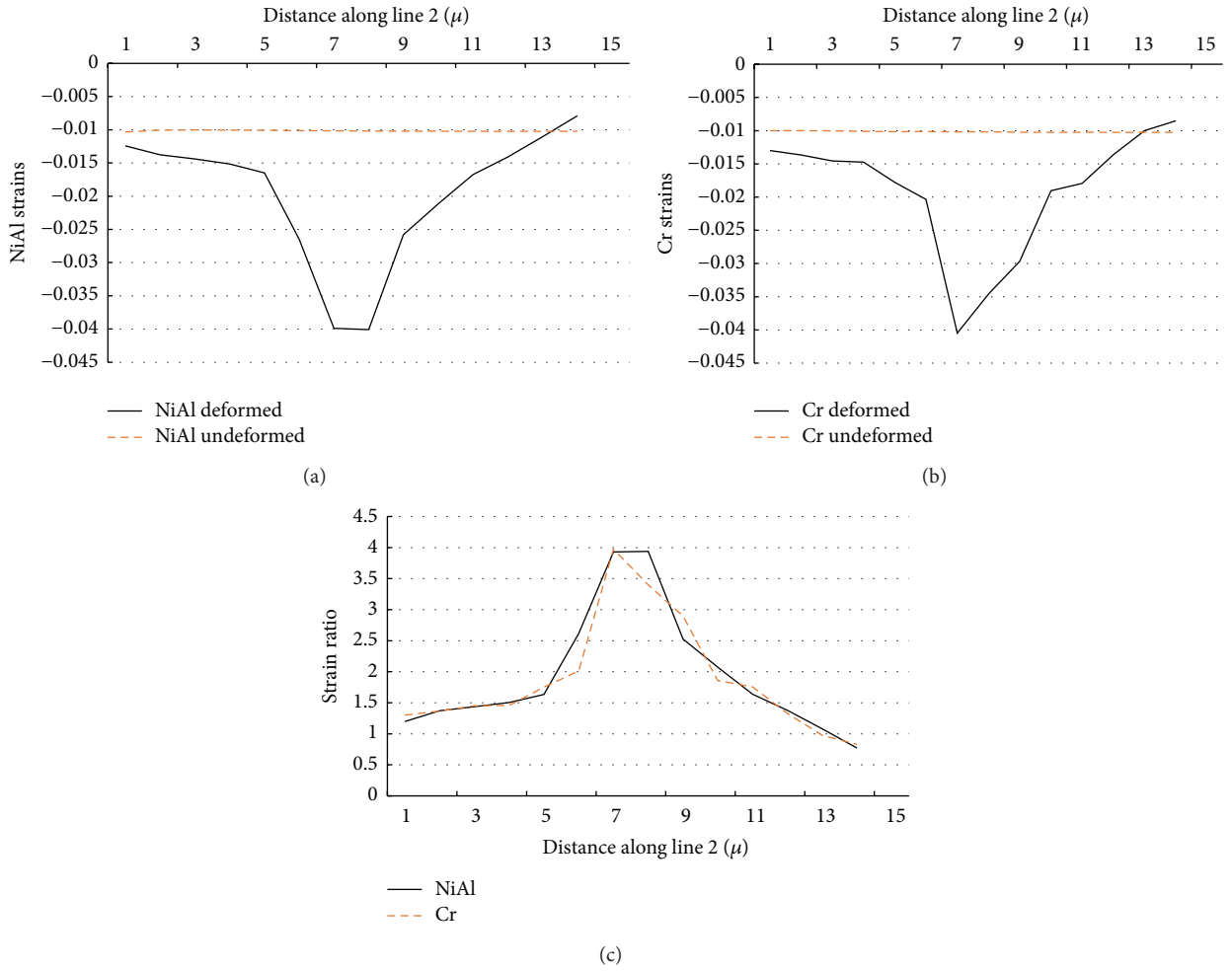

Figure 11: Strains and strain ratio for Cr and NiAl lamellae along line 2 shown in Figure 9: (a) strain in an NiAl layer as a function of position; (b) strain in a Cr layer as a function of position; (c) strain ratio for NiAl and Cr lamellae as a function of position.

and softer parts of the composite. These results provide new insights into the strain partitioning and the role of interfaces in this nanocomposite.

Competing Interests

The authors declare that they have no competing interests.

Acknowledgments

Research was sponsored by the Laboratory Directed Research and Development Program of Oak Ridge National Laboratory, managed by UT-Battelle, LLC, for the US Department of Energy, and the funding from the NSF I/UCRC (IIP-1362146) grant. Use of the Advanced Photon Source was supported by the US Department of Energy, Office of Science, Office of Basic Energy Sciences, under Contract no. DE-AC02-06CH11357. Data was collected on beamline 34ID-E at the Advanced Photon Source, Argonne National Laboratory. The authors would also like to thank the Private Sector Program at the National Center for Supercomputing Applications (NCSA) for its computational and software resources. The authors thank H. Bei (ORNL) for sample preparation.

References

[1] C. Dietrich, M. H. Poech, H. F. Fischmeister, and S. Schmauder, "Stress and strain partitioning in a Ag-Ni fibre composite under transverse loading Finite element modelling and experimental study," *Computational Materials Science*, vol. 1, no. 3, pp. 195–202, 1993.

[2] J. Wang, R. G. Hoagland, and A. Misra, "Mechanics of nanoscale metallic multilayers: from atomic-scale to micro-scale," *Scripta Materialia*, vol. 60, no. 12, pp. 1067–1072, 2009.

[3] K. Dannemann, N. S. Stoloff, and D. J. Duquette, "High temperature fatigue of three nickel-base eutectic composites," *Materials Science and Engineering*, vol. 95, pp. 63–71, 1987.

[4] A. Needleman, "Computational mechanics at the mesoscale," *Acta Materialia*, vol. 48, no. 1, pp. 105–124, 2000.

[5] G. Frommeyer and R. Rablbauer, "High temperature materials based on the intermetallic compound NiAI reinforced by

refractory metals for advanced energy conversion technologies," *Steel Research International*, vol. 79, no. 7, pp. 507–512, 2008.

[6] J. W. Hutchinson and A. G. Evans, "Mechanics of materials: top-down approaches to fracture," *Acta Materialia*, vol. 48, no. 1, pp. 125–135, 2000.

[7] A. G. Evans, "Design and life prediction issues for high-temperature engineering ceramics and their composites," *Acta Materialia*, vol. 45, no. 1, pp. 23–40, 1997.

[8] Y. Li, Z. Zhang, R. Vogt, J. M. Schoenung, and E. J. Lavernia, "Boundaries and interfaces in ultrafine grain composites," *Acta Materialia*, vol. 59, no. 19, pp. 7206–7218, 2011.

[9] I. J. Beyerlein, N. A. Mara, D. Bhattacharyya, D. J. Alexander, and C. T. Necker, "Texture evolution via combined slip and deformation twinning in rolled silver-copper cast eutectic nanocomposite," *International Journal of Plasticity*, vol. 27, no. 1, pp. 121–146, 2011.

[10] D. Yu, H. Bei, Y. Chen, E. P. George, and K. An, "Phase-specific deformation behavior of a relatively tough NiAl–Cr(Mo) lamellar composite," *Scripta Materialia*, vol. 84-85, pp. 59–62, 2014.

[11] R. I. Barabash, W. Liu, J. Z. Tischler, H. Bei, and J. D. Budai, "Phase-specific elastic/plastic interface interactions in layered NiAl–Cr(Mo) structures," *Acta Materialia*, vol. 60, no. 8, pp. 3279–3286, 2012.

[12] R. I. Barabash, H. Bei, Y. F. Gao, and G. E. Ice, "Interface strength in NiAl-Mo composites from 3-D X-ray microdiffraction," *Scripta Materialia*, vol. 64, no. 9, pp. 900–903, 2011.

[13] G. Frommeyer, R. Rablbauer, and H. J. Schäfer, "Elastic properties of B2-ordered NiAl and NiAl–X (Cr, Mo, W) alloys," *Intermetallics*, vol. 18, no. 3, pp. 299–305, 2010.

[14] H. Bei, E. P. George, and G. M. Pharr, "Small-scale mechanical behavior of intermetallics and their composites," *Materials Science and Engineering A*, vol. 483-484, no. 1-2, pp. 218–222, 2008.

[15] J. M. Tartaglia and N. S. Stoloff, "Fatigue of Ni-Al-Mo aligned eutectics at elevated temperatures," *Metallurgical Transactions A*, vol. 12, no. 11, pp. 1891–1898, 1981.

[16] R. Rablbauer, G. Frommeyer, and F. Stein, "Determination of the constitution of the quasi–binary eutectic NiAl–Re system by DTA and microstructural investigations," *Materials Science and Engineering A*, vol. 343, no. 1-2, pp. 301–307, 2003.

[17] J. T. Guo, K. W. Huai, Q. Gao, W. L. Ren, and G. S. Li, "Effects of rare earth elements on the microstructure and mechanical properties of NiAl-based eutectic alloy," *Intermetallics*, vol. 15, no. 5-6, pp. 727–733, 2007.

[18] L.-Z. Tang, Z.-G. Zhang, S.-S. Li, and S.-K. Gong, "Mechanical behaviors of NiAl-Cr(Mo)-based near eutectic alloy with Ti, Hf, Nb and W additions," *Transactions of Nonferrous Metals Society of China*, vol. 20, no. 2, pp. 212–216, 2010.

[19] L. Y. Sheng, W. Zhang, J. T. Guo, L. Z. Zhou, and H. Q. Ye, "Microstructure evolution and mechanical properties' improvement of NiAl–Cr(Mo)–Hf eutectic alloy during suction casting and subsequent HIP treatment," *Intermetallics*, vol. 17, no. 12, pp. 1115–1119, 2009.

[20] L. Y. Sheng, Y. Xie, T. F. Xi, J. T. Guo, Y. F. Zheng, and H. Q. Ye, "Microstructure characteristics and compressive properties of NiAl-based multiphase alloy during heat treatments," *Materials Science and Engineering A*, vol. 528, no. 29-30, pp. 8324–8331, 2011.

[21] K. Huai, J. Guo, Z. Ren, Q. Gao, and R. Yang, "Effect of Nb on the microstructure and mechanical properties of cast NiAl-Cr(Mo) eutectic alloy," *Journal of Materials Science and Technology*, vol. 22, no. 2, pp. 164–168, 2006.

[22] J.-M. Yang, S. M. Jeng, K. Bain, and R. A. Amato, "Microstructure and mechanical behavior of in-situ directional solidified NiAl/Cr(Mo) eutectic composite," *Acta Materialia*, vol. 45, no. 1, pp. 295–305, 1997.

[23] R. I. Barabash and G. E. Ice, Eds., *Strain and Dislocation Gradients from Diffraction*, Imperial College Press, London, UK, 1st edition, 2014.

[24] R. Barabash, G. E. Ice, B. C. Larson, G. M. Pharr, K.-S. Chung, and W. Yang, "White microbeam diffraction from distorted crystals," *Applied Physics Letters*, vol. 79, no. 6, pp. 749–751, 2001.

[25] W. Yang, B. C. Larson, G. E. Ice et al., "Spatially resolved poisson strain and anticlastic curvature measurements in Si under large deflection bending," *Applied Physics Letters*, vol. 82, no. 22, pp. 3856–3858, 2003.

[26] G. E. Ice, J. D. Budai, and J. W. L. Pang, "The race to X-ray microbeam and nanobeam science," *Science*, vol. 334, no. 6060, pp. 1234–1239, 2011.

[27] L. Wang, R. Barabash, T. Bieler, W. Liu, and P. Eisenlohr, "Study of 11-2 1 twinning in α-Ti by EBSD and laue microdiffraction," *Metallurgical and Materials Transactions A*, vol. 44, no. 8, pp. 3664–3674, 2013.

[28] R. I. Barabash, O. M. Barabash, M. Ojima et al., "Interphase strain gradients in multilayered steel composite from microdiffraction," *Metallurgical and Materials Transactions A*, vol. 45, no. 1, pp. 98–108, 2014.

[29] Abaqus, *Abaqus/Standard Analysis User's Manual, Version 6.13*, 2013.

[30] S. Koric and B. G. Thomas, "Efficient thermo-mechanical model for solidification processes," *International Journal for Numerical Methods in Engineering*, vol. 66, no. 12, pp. 1955–1989, 2006.

[31] C. Zienkiewicz and L. T. Taylor, *The Finite Element Method for Fluid Dynamics*, Butterworth-Heinemann, Boston, Mass, USA; Elsevier, Burlington, Mass, USA, 6th edition, 2005.

[32] S. Koric, Q. Lu, and E. Guleryuz, "Evaluation of massively parallel linear sparse solvers on unstructured finite element meshes," *Computers and Structures*, vol. 141, pp. 19–25, 2014.

[33] J. Fish and T. Belytschko, *A First Course in Finite Elements*, John Wiley & Sons, Chichester, UK, 2007.

[34] iForge, *iForge-NCSA's Exclusive Industrial HPC Resource*, 2013, http://www.ncsa.illinois.edu/News/12/0709NCSAiForge.html.